Article

Ferromagnetic Resonance of a [GeTe/Sb$_2$Te$_3$]$_6$/Py Superlattice

Satoshi Sumi [1,*], Yuichiro Hirano [1], Hiroyuki Awano [1] and Junji Tominaga [2]

[1] Department of Advanced Science and Technology, Toyota Technological Institute, Nagoya 468-8511, Japan; Hirano.sd16429@gmail.com (Y.H.); awano@toyota-ti.ac.jp (H.A.)
[2] Device Technology Research Institute, National Institute of Advanced Industrial Science and Technology (AIST), Tsukuba 305-8565, Japan; j-tominaga@aist.go.jp
*   Correspondence: sumi@toyota-ti.ac.jp

Abstract: A [GeTe/Sb$_2$Te$_3$] superlattice is known as a topological insulator. It shows magnetic responses such as magneto-optical effect, magneto resistance, magneto capacitance, and so on. We have reported that [GeTe/Sb$_2$Te$_3$] superlattice film has a large spin–orbit interaction using a spin pumping method of a [GeTe/Sb$_2$Te$_3$]/Py superlattice. In this paper, we demonstrate a ST-FMR (spin transfer torque ferromagnetic resonance) of the [GeTe/Sb$_2$Te$_3$]$_6$/Py superlattice, compared with a W/Py bilayer. The superlattice film showed a large resonance signal with a symmetric component. The ratio of symmetric components (S) to anti-symmetric (A) components (S/A) was 1.4, which suggests that the superlattice exhibits a large spin Hall angle. The [GeTe/Sb$_2$Te$_3$] superlattice will be suitable as a hetero-interface material required for high performance spintronics devices in future.

Keywords: topological insulator; superlattice; ST-FMR; spin Hall angle; spintronics

1. Introduction

Topological insulators (TIs) have attracted much attention for spintronics devices and their physical origin [1–5]. Tis, such as chalcogenides of Sb$_2$Te$_3$ built from quintuple layers (QL) of Te-Sb-Te-Sb-Te, satisfy both spatial inversion symmetry and time reversal symmetry because of a single Dirac cone at the Γ point [6–8]. The spin bands are degenerated by the inversion symmetry. However, the spatial symmetry is broken, for example, by an external electric field, the band gap opens, and the spin degeneracy is resolved by a Rashba-split phase [9]. In a surface state of the TIs, a spin–orbit interaction (SOI) is maximal when an electron's spin orientation is fixed relative to its propagation direction [10–12]. We can determine the strength of the SOI by using a spin torque ferromagnetic resonance (ST-FMR) technique [13]. In the ST-FMR, rf current induced spin currents and caused resistance oscillations due to the magnetoresistance of a ferromagnetic layer. We can measure the SOI from the resonance curve of a direct voltage, which is caused by mixing the applied rf current and the oscillating resistance.

[GeTe/Sb$_2$Te$_3$] superlattice films are known as an interfacial phase change memory material, which was originally developed to reduce the switching energy consumption in phase-change random access memory (PRAM) [14,15]. The films consist of a superlattice with Sb$_2$Te$_3$ (TI) and normal insulator GeTe (NI), which have two phases of a topological insulator (RESET phase) and normal insulator (SET phase) [16,17]. Recently, it was reported that the film shows magnetic properties, such as magneto-resistance, Kerr effect, magneto-capacitance, etc. The magneto-resistance of the films was over 2000% at room temperature under a magnetic field of 1 kOe [18]. Moreover, the films showed a large mirror-symmetric magneto-optical Kerr effect and a magneto-capacitance at the SET phase [19,20]. The origin of the magnetic sensitivity is due to the p_z-electrons of Ge and Te atoms in the Ge$_2$Te$_2$ layers of the superlattice [16]. In addition, it was clear using ab-initio simulations that the film is a topological insulator with a strong SOI [21]. Moreover, the films showed a topologically protected spin diffusion length of more than 100 µm at room temperature [22].

We also confirmed that there exists a large SOI in a [GeTe/Sb$_2$Te$_3$]/Py superlattice, by a spin pumping method using Electron Spin Resonance (ESR). The width of the FMR spectrum was broadened by the strong SOI and a damping coefficient was as large as 0.027 [23].

In this paper, we demonstrate the SOI of the [GeTe/Sb$_2$Te$_3$]$_6$ superlattice film by an ST-FMR of the [GeTe/Sb$_2$Te$_3$]$_6$/Ni$_{80}$Fe$_{20}$ (Py) bilayer. The film shows a strong SOI, and we estimated a large spin Hall angle for the [GeTe/Sb$_2$Te$_3$] superlattice film.

2. Methods

2.1. Fabrication of the Films

We measured two samples of [GeTe/Sb$_2$Te$_3$]$_6$/Py and W/Py films. Here, the W/Py film was prepared for a control sample. The sample structures are shown in Figure 1. The [GeTe/Sb$_2$Te$_3$]$_6$/Py film was fabricated on a crystalline sapphire substrate <0001> using a sputtering system. The GeTe, Sb$_2$Te$_3$ and Py films were sputtered from the GeTe, Sb$_2$Te$_3$ and Ni$_{80}$Fe$_{20}$ alloy targets, respectively. The unit thickness of the (GeTe)$_2$ and (Sb$_2$Te$_3$)$_1$ layers were 0.85 nm and 1.0 nm, respectively. The unit thickness of the (GeTe)$_2$ is two monolayers of (GeTe), and the unit thickness of the (Sb$_2$Te$_3$)$_1$ is one monolayer of (Sb$_2$Te$_3$). The bilayer of a [(GeTe)$_2$/(Sb$_2$Te$_3$)$_1$] was stacked 6 times. The structure is same as previous reports [22]. To ensure a strong crystalline orientation, a 20 nm-thick amorphous Si and a 3 nm-thick Sb$_2$Te$_3$ layer were formed prior to the deposition of the films as seed layers. A 5 nm-thick Sb$_2$Te$_3$ layer was finally deposited on the top as a protective layer. We can obtain a well ordered superlattice using this method [24,25]. Finally, a 60 nm-thick Py layer was deposited as a magnetic resonance layer and an electrode used in FMR/ST-FMR. The thicknesses were determined with the deposition rate of each target and the compositions with composition of each target. The film was patterned using metal stencils with a size of 1.5 mm width and 7 mm length for the superlattice, and with a size of 0.1 mm width and 3 mm length for the Py layer. The control sample of W/Py film was prepared to insert an 18 nm-thick W layer between the amorphous Si and the Py layers instead of the superlattice. The W layer was sputtered using a W target. The resistivities of the Py, W and superlattice films, measured with the 4 probes method, are 8.9×10^{-7} Ωm, 2.2×10^{-7} Ωm and 3.3×10^{-5} Ωm, respectively.
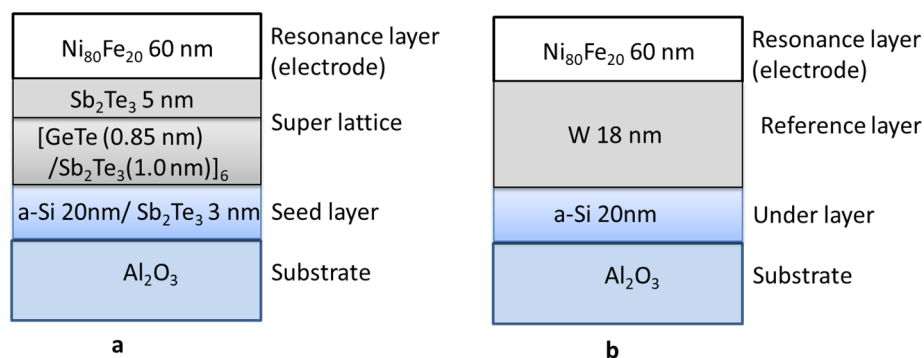

Figure 1. Sample structures of (**a**) a [GeTe/Sb$_2$Te$_3$]$_6$/Py superlattice film and (**b**) control sample of a W/Py film.

2.2. Measurement

FMR and ST-FMR measurement setups are shown in Figure 2a,b, respectively. In the normal FMR measurement, RF signals from a signal generator (Agilent model 83620B) with a frquency range of 5 to 9 GHz were applied to the samples through a directional coupler (Agilent model 8472B). The RF signal amplitude was modulated with a frequency of 1 KHz for a Lock-in detection. The reflection signals were separated by the coupler and detected by a Lock-in amplifier (model SR830, Stanford, Sunnyvale, CA, USA) through a Schottky diode detector (model 87300B, Keysight, Santa Rosa, CA, USA). In the ST-FMR

measurement, RF signals were applied to the samples and DC components were detected by a Lock-in amplifier through a bias T (Picosecond model 5575A). Input RF powers for the samples were 7 dBm for all the measurements. In the FMR, we applied the magnetic field parallel to the rf current (normal to the rf field). On the other hand, in the ST-FMR, we applied the magnetic field 45 degrees to the rf current to induce a resistance oscillation due to the anisotropic magnetoresistance in the Py [13].
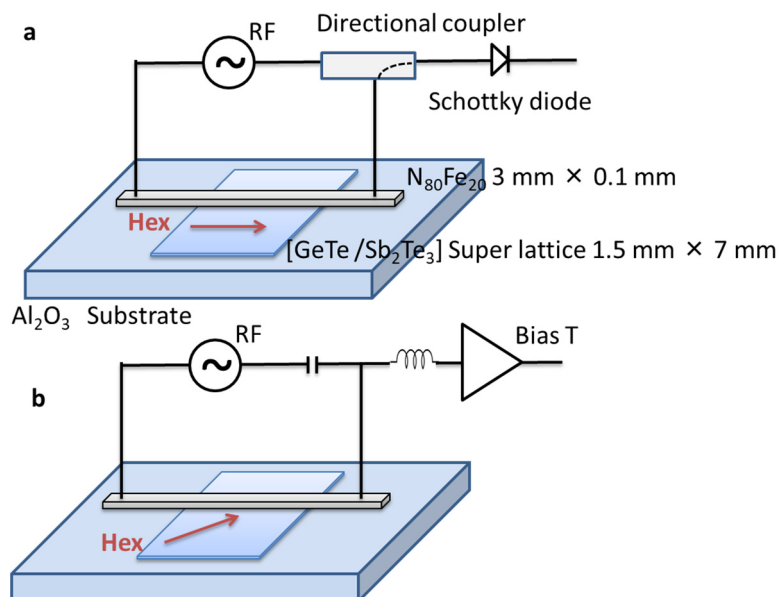

Figure 2. Schematic diagram of setups for (**a**) normal FMR and (**b**) ST-FMR. For the normal FMR, RF signals with a frequency range of 5 to 9 GHz were applied to the film. Reflection signals were detected through a directional coupler by a Lock-in amplifier. For the ST-FMR, RF signal with a frequency of 7 GHz was applied to the film and DC components were detected by a Lock-in amplifier through a bias T. The external field was applied at 0 degrees for the normal FMR and 45 degrees for the ST-FMR from the direction of applied current.

In the normal FMR, the RF current generates Oersted fields, which are driving magnetization precessions in the Py layer. At the ferromagnetic resonance field, the RF signal is absorbed by the Py. Therefore, we can detect a FMR through the reflection of RF signal from the sample. In the ST-FMR, the RF current in the $[\text{GeTe/Sb2Te3}]_6$ or the W layer injects a spin current into the Py layer as well as Oersted fields, which drives magnetization precessions in the Py layer. The magnetization precessions result in an oscillation of the resistance through the anisotropic magnetoresistance in the Py layer. We can detect a mixing DC voltage of symmetric and anti-symmetric Lorentzian functions using the bias T [26,27].

3. Results

3.1. Normal FMR

Figure 3a shows a normal FMR from the $[\text{GeTe/Sb}_2\text{Te}_3]_6/\text{Py}$ film at a frequency of 7 GHz. The horizontal axis shows an applied magnetic field, and the vertical axis shows reflection RF signal amplitudes from the film. There is a report about the strong contribution of eddy currents in the FMR [28]. As the skin depth of the microwave frequencies is thought to be small in this sample, we can clearly see an absorption of the ferromagnetic resonance. It was observed around external fields of 550 Oe, which was almost the same as that of a pure Py. It was increased with increasing the RF frequency. Figure 3b shows a resonance frequency as a function of the field. The relationship was consistent with the Kittle formula $f_{res} = (\gamma/2\pi)[H_{res}(H_{res} + 4\pi M_s]^{1/2}$ with a parameter of Py, where γ is gyromagnetic ratio

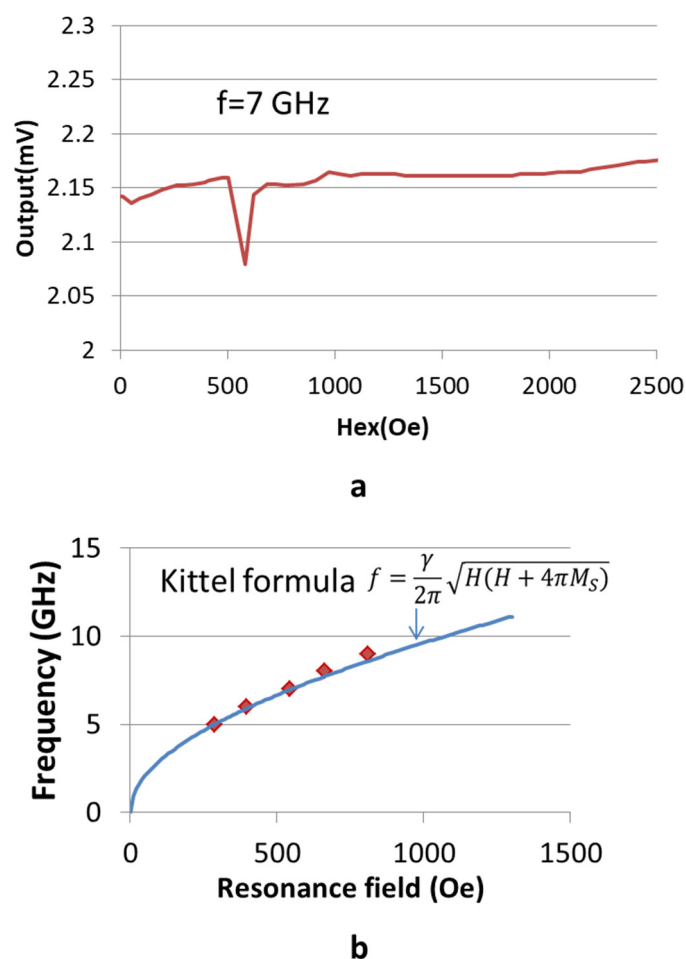and M_s is 670 emu/cc for the Py [29]. Therefore, it was found that the resonances were caused by the Py layer.

Figure 3. Normal FMR for the [GeTe/Sb$_2$Te$_3$]$_6$/Py film. (**a**) A resonance spectrum at 7 GHz and (**b**) a resonance frequency as a function of a field. Dots show experimental results and a line shows Kittel formula fitting.

3.2. ST-FMR

Figure 4 shows the ST-FMR spectrum of (a) the [GeTe/Sb$_2$Te$_3$]$_6$/Py sample and (b) the W/Py sample at a frequency of 7 GHz. The horizontal axis shows an applied magnetic field, and the vertical axis shows a mixing DC voltage caused by the ferromagnetic resonance. Standard deviations of the noise are 7.1 nV for (a) and 9.2 nV for (b). In the former sample, a large DC component of the resonance was detected at the resonance frequency of Py. The signal was high and symmetrical. The ST-FMR of the single Py film shows only a small peak around the resonance field of 500 Oe. The large DC component is thought to be generated by the [GeTe/Sb$_2$Te$_3$]$_6$ film. In the latter control sample, on the other hand, although a signal was detected at the same frequency, the amplitude was relatively small. From the X-ray diffraction (XRD), the W film had an α-W phase, which is known to show a smaller SHE than that of a β-W [30,31]. Therefore, the amplitude was thought to be small. The superlattice sample had a larger SHE than that of the control.
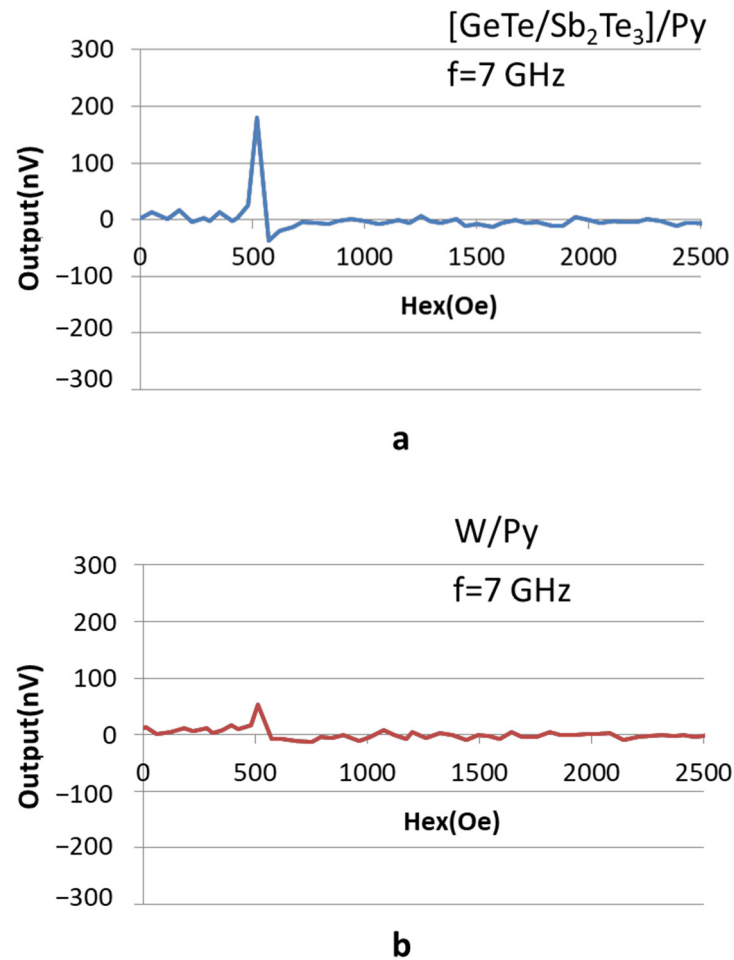
Figure 4. ST-FMR spectrum with a frequency of 7GHz. (**a**) [GeTe/Sb$_2$Te$_3$]$_6$/Py superlattice and (**b**) control sample of W/Py film.

In the ST-FMR, the resonance curve has symmetric and anti-symmetric components, which correspond to spin current-induced FMR and Oersted filed-induced FMR. It follows in the next equation [32,33]:

$$V_{mix} = S\frac{\Delta H^2}{\Delta H^2 + (H_{ext} - H_{res})^2} + A\frac{\Delta H(H_{ext} - H_{res})}{\Delta H^2 + (H_{ext} - H_{res})^2} \qquad (1)$$

The values of S and A, the resonance field (H_{res}) and the half linewidth (ΔH) are obtained by fitting V_{mix} with symmetric and anti-symmetric Lorentzian functions. H_{ext} are applied in the external field. Additionally, the origins of spin currents are not clear in the [GeTe/Sb$_2$Te$_3$]$_6$/Py film. We fitted the ST-FMR results using Equation (1). Figure 5a shows the fitting results of a symmetric Lorentzian function (S), an anti-symmetric Lorentzian function (A) and V_{mix} ($S + A$) for the superlattice sample, and Figure 5b shows V_{mix} ($S + A$) and the experimental result. The horizontal axis shows an applied magnetic field, and the vertical axis shows the DC voltages for each components. The resonance curve could be divided into a symmetric (S) and an anti-symmetric (A) Lorentzian function. The fitting V_{mix} ($S + A$) curve was well consistent with the experimental result. The S/A ratio of the superlattice sample was 1.4, which is a very large value, in the case of the control sample, as the ratio of the α-W phase is considered to be small among heavy metals. Therefore, it was hard to fit the functions due to the weak signal.
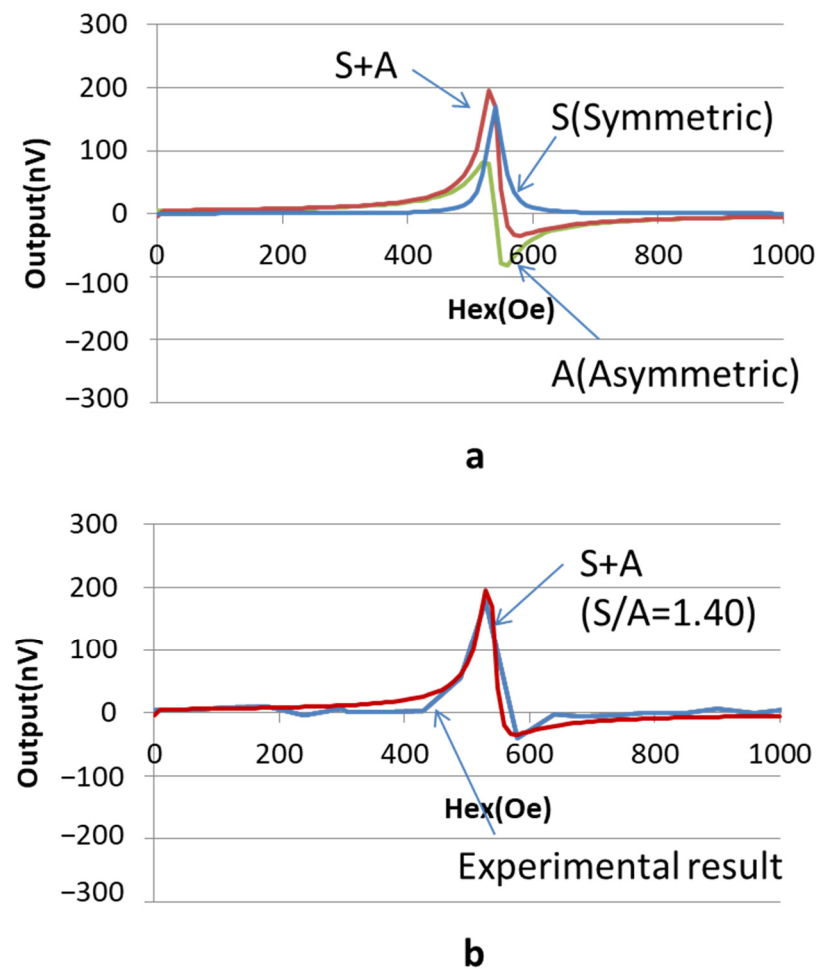
Figure 5. Fitting results of a symmetric Lorentzian function (*S*), an anti-symmetric Lorentzian function (*A*) and V_{mix} (*S* + *A*) for the superlattice sample at 7 GHz. (**a**) A symmetric component S, an anti-symmetric component *A* and V_{mix} of *S* + *A*, (**b**) V_{mix} of *S* + *A* (red line) and the experimental result (blue line).

4. Discussions

Spin Hall angle (SHA) is the ratio of the spin current density to the RF current density. It means a conversion ratio of the spin current to charge current. In the TI surface, a spin current converts to a charge current through the SOI. It is known that SHA is proportional to the symmetric and anti-symmetric component ratio of Equation (1) [32,33]. The SHA is given by

$$\theta_{SH}^{ST} = \frac{S}{A} \frac{e\mu_0 M_S t d}{h} \left[1 + \left(\frac{4\pi M_{eff}}{H_{res}} \right) \right]^{1/2}. \tag{2}$$

where e, η_0, h, H_{res}, M_s, M_{eff}, t and d are elementary charge, permeability in vacuum, Planck constant, the resonance field, saturation magnetization, effective magnetization, and each layer thickness, respectively.

In this equation, SHA depends on the thickness of each layer. Although it is hard to determine a conduction layer thickness of the [GeTe/Sb$_2$Te$_3$]$_6$ superlattice with the Sb$_2$Te$_3$ protective layer, assuming the SHE layer thickness to be 6 nm (Sb$_2$Te$_3$ layer thickness in the superlattice), the SHA value can be estimated as 1.3, where S/A, H_{res}, M_s, d are 1.4, 550 Oe, 670 emu/cc, 60 nm, respectively, and M_{eff} assumes the same as M_s. The SHA is 0.08 for typical materials of heavy metal Pt [26] and less than 0.07 for α-W [31]. Due to the result, it is supposed that the [GeTe/Sb$_2$Te$_3$]$_6$ superlattice has an extremely large SOI, which may be related to the special properties of topological insulator [34].

In summary, we demonstrated ST-FMR of $[GeTe/Sb_2Te_3]_6/Py$ superlattice. The superlattice film showed a large resonance signal with a symmetric component. The ratio of S/A, the symmetric S to anti-symmetric A components, was 1.4. This value suggests that the superlattice exhibits a large spin Hall angle. We conclude that $[GeTe/Sb_2Te_3]_6$ superlattice has a large spin orbit interaction, although neither the elements of Ge, Sb nor Te are non-magnetic materials.

We believe that the superlattices will be promising materials for future spintronics devices.

Author Contributions: J.T. and H.A. planned the study. J.T. prepared the films. S.S. and Y.H. measured the FMR and analyzed the results with inputs from H.A. and J.T. All authors have read and agreed to the published version of the manuscript.

Data Availability Statement: Data is contained within the article.

Conflicts of Interest: The authors declare no conflict of interest.

References

1. Moore, J.E. The birth of topological insulator. *Nature* **2010**, *464*, 194–198. [CrossRef] [PubMed]
2. Bernevig, B.A.; Hughes, T.L.; Zhang, S.-C. Topological Phase Transition in HgTe Quantum Wells. *Science* **2006**, *314*, 1757–1761. [CrossRef] [PubMed]
3. Hsieh, D.; Qian, D.; Wray, L.; Xia, Y.; Hor, Y.S.; Cava, R.J.; Hasan, M.Z. A topological Dirac insulator in a quantum spin Hall phase. *Nature* **2008**, *452*, 970–974. [CrossRef] [PubMed]
4. Xia, Y.; Qian, D.; Hsieh, D.; Wray, L.A.; Pal, A.; Lin, H.; Bansil, A.; Grauer, D.; Hor, Y.S.; Cava, R.J.; et al. Observation of a large-gap topological-insulator class with a single Dirac cone on the surface. *Nat. Phys.* **2009**, *5*, 398–402. [CrossRef]
5. Hsieh, D.; Xia, Y.; Qian, D.; Wray, L.; Dil, J.H.; Meier, F.; Osterwalder, J.; Patthey, L.; Checkelsky, J.G.; Ong, N.P.; et al. A tunable topological insulator in the spin helical Dirac transport regime. *Nature* **2009**, *460*, 1101–1106. [CrossRef]
6. Hsieh, D.; Xia, Y.; Qian, D.; Wray, L.; Meier, F.; Dil, J.H.; Osterwalder, J.; Patthey, L.; Fedorov, A.V.; Lin, H.; et al. Observation of time-reversal-projected single-Dirac-cone topological-insulator states in Bi_2Te_3 and Sb_2Te_3. *Phys. Rev. Lett.* **2009**, *103*, 146401. [CrossRef] [PubMed]
7. Zhang, H.; Liu, C.-X.; Qi, X.-L.; Dai, X.; Fang, Z.; Zhang, S.-C. Topological insulators in Bi_2Se_3, Bi_2Te_3 and Sb_2Te_3 with a single Dirac cone on the surface. *Nat. Phys.* **2009**, *5*, 438–442. [CrossRef]
8. Kifune, K.; Kubota, Y.; Matsunaga, T.; Yamada, N. Extremely long period-stacking structure in the Sb–Te binary system. *Acta Crystallogr. Sect. B Struct. Sci.* **2005**, *61*, 492–497. [CrossRef]
9. Kim, M.; Kim, C.H.; Kim, H.-S.; Ihm, J. Topological quantum phase transitions driven by external electric fields in Sb_2Te_3 thin films. *Proc. Natl. Acad. Sci. USA* **2012**, *109*, 671–674. [CrossRef]
10. Burkov, A.A.; Hawthorn, D.G. Spin and Charge Transport on the Surface of a Topological Insulator. *Phys. Rev. Lett.* **2010**, *105*, 066802. [CrossRef] [PubMed]
11. Culcer, D.; Hwang, E.H.; Stanescu TDSarma, S.D. Two-dimensional surface charge transport in topological insulators. *Phys. Rev. B* **2010**, *82*, 155457. [CrossRef]
12. Pesin, D.; MacDonald, A. Spintronics and pseudospintronics in graphene and topological insulators. *Nat. Mater.* **2012**, *11*, 409–416. [CrossRef] [PubMed]
13. Mellnik, A.R.; Lee, J.S.; Richardella, A.; Grab, J.; Mintun, P.J.; Fischer, M.H.; Vaezi, A.; Manchon, A.; Kim, E.-A.; Samarth, N.; et al. Spin-transfer torque generated by a topological insulator. *Nat. Cell Biol.* **2014**, *511*, 449–451. [CrossRef] [PubMed]
14. Gervacio-Arciniega, J.J.; Prokhorov, E.; Espinoza-Beltrán, F.J.; Trapaga, G. Characterization of local piezoelectric behavior of ferroelectric GeTe and $Ge_2Sb_2Te_5$ thin films. *J. Appl. Phys.* **2012**, *112*, 052018. [CrossRef]
15. E Simpson, R.; Fons, P.; Kolobov, A.V.; Fukaya, T.; Krbal, M.; Yagi, T.; Tominaga, J. Interfacial phase-change memory. *Nat. Nanotechnol.* **2011**, *6*, 501–505. [CrossRef]
16. Tominaga, J.; Kolobov, A.V.; Fons, P.J.; Wang, X.; Saito, Y.; Nakano, T.; Hase, M.; Murakami, S.; Herfort, J.; Takagaki, Y.; et al. Giant multiferroic effects in topological $GeTe$-Sb_2Te_3 superlattices. *Sci. Technol. Adv. Mater.* **2015**, *16*, 014402. [CrossRef] [PubMed]
17. Tominaga, J.; Kolobov, A.V.; Fons, P.; Nakano, T.; Murakami, S. Ferroelectric Order Control of the Dirac-Semimetal Phase in $GeTe$-Sb_2Te_3 Superlattices. *Adv. Mater. Interfaces* **2014**, *1*, 1300027. [CrossRef]
18. Tominaga, J.; Simpson, R.E.; Fons, P.; Kolobov, A.V. Electrical-field induced giant magnetoresistivity in (non-magnetic) phase change films. *Appl. Phys. Lett.* **2011**, *99*, 152105. [CrossRef]
19. Bang, D.; Awano, H.; Tominaga, J.; Kolobov, A.V.; Fons, P.; Saito, Y.; Makino, K.; Nakano, T.; Hase, M.; Takagaki, Y.; et al. Mirror-symmetric Magneto-optical Kerr Rotation using Visible Light in $[(GeTe)_2(Sb_2Te_3)_1]_n$ Topological Superlattices. *Sci. Rep.* **2014**, *4*, 5727. [CrossRef]

20. Sumi, S.; Awano, H.; Tominaga, J. *Magneto-Capacitance of [GeTe/Sb$_2$Te$_3$] Supper Lattice Film*; e-PCOS 2017 PC-09; Aachen, Germany, 2017.

21. Sa, B.; Zhou, J.; Sun, Z.; Tominaga, J.; Ahuja, R. Topological Insulating in GeTe/Sb$_2$Te$_3$ Phase-Change Superlattice. *Phys. Rev. Lett.* **2012**, *109*, 096802. [CrossRef]

22. Tominaga, J.; Miyata, N.; Sumi, S.; Awano, H.; Murakami, S. Topologically protected spin diffusion and spin generator using chalcogenide superlattices. *NPJ 2D Mater. Appl.* **2020**, *4*, 22. [CrossRef]

23. Hirano, Y.; Sumi1, S.; Bang, D.; Awano, H.; Saito, Y.; Tominaga, J. *Damping Coefficient Enhancement Evidence for Spin Orbit Interaction on [(GeTe)$_2$/(Sb$_2$Te$_3$)$_1$]20 Superlattices*; Moris2018 TuP-19; New York, NY, USA, 2018.

24. Tominaga, J. The Design and Application on Interfacial Phase-Change Memory. *Phys. Status Solidi (RRL)-Rapid Res. Lett.* **2019**, *13*, 1800539. [CrossRef]

25. Tominaga, J.; Sumi, S.; Awano, H. Intermixing suppression through the interface in GeTe/Sb$_2$Te$_3$ superlattice. *Appl. Phys. Express* **2020**, *13*, 075503. [CrossRef]

26. Liu, L.; Moriyama, T.; Ralph, D.C.; Buhrman, R.A. Spin-Torque Ferromagnetic Resonance Induced by the Spin Hall Effect. *Phys. Rev. Lett.* **2011**, *106*, 036601. [CrossRef] [PubMed]

27. Pai, C.-F.; Ou, Y.; Vilela-Leão, L.H.; Ralph, D.C.; Buhrman, R.A. Dependence of the efficiency of spin Hall torque on the transparency of Pt/ferromagnetic layer interfaces. *Phys. Rev. B* **2015**, *92*, 064426. [CrossRef]

28. Maksymov, I.S.; Zhang, Z.; Chang, C.; Kostylev, M. Strong Eddy-Current Shielding of Ferromagnetic Resonance Response in Sub-Skin-Depth-Thick Conducting Magnetic Multilayers. *IEEE Mag. Lett.* **2014**, *5*, 3500104. [CrossRef]

29. Kittel, C. On the Theory of Ferromagnetic Resonance Absorption. *Phys. Rev.* **1948**, *73*, 155–161. [CrossRef]

30. Mondal, S.; Choudhury, S.; Jha, N.; Ganguly, A.; Sinha, J.; Barman, A. All-optical detection of the spin Hall angle in W/CoFeB/SiO$_2$ heterostructures with varying thickness of the tungsten layer. *Phys. Rev. B* **2017**, *96*, 054414. [CrossRef]

31. Pai, C.-F.; Liu, L.; Li, Y.; Tseng, H.W.; Ralph, D.C.; Buhrman, R.A. Spin transfer torque devices utilizing the giant spin Hall effect of tungsten. *Appl. Phys. Lett.* **2012**, *101*, 122404. [CrossRef]

32. Zhang, W.; Han, W.; Jiang, X.; Yang, S.H.; Parkin, S.S.P. Role of transparency of platinum–ferromagnet interfaces in determining the intrinsic magnitude of the spin Hall effect. *Nat. Phys.* **2015**, *11*, 496–502. [CrossRef]

33. Kondou, K.; Yoshimi, R.; Tsukazaki, A.; Fukuma, Y.; Matsuno, J.; Takahashi, K.S.; Kawasaki, M.; Tokura, Y.; Otani, Y. Fermi-level-dependent charge-to-spin current conversion by Dirac surface states of topological insulators. *Nat. Phys.* **2016**, *12*, 1027–1031. [CrossRef]

34. Khang, N.H.D.; Ueda, Y.; Hai, P.N. A conductive topological insulator with large spin Hall effect for ultralow power spin–orbit torque witching. *Nat. Mater.* **2018**, *17*, 808–813. [CrossRef] [PubMed]